

SEP-YOLO: Fourier-Domain Feature Representation for Transparent Object Instance Segmentation

Fengming Zhang
Jiangnan University
Wuxi, China

6233110051@stu.jiangnan.edu.cn

Tao Yan*
Jiangnan University
Wuxi, China
yantao@jiangnan.edu.cn

Jianchao Huang
Jiangnan University
Wuxi, China
6233112018@stu.jiangnan.edu.cn

Abstract—Transparent object instance segmentation presents significant challenges in computer vision, due to the inherent properties of transparent objects, including boundary blur, low contrast, and high dependence on background context. Existing methods often fail as they depend on strong appearance cues and clear boundaries. To address these limitations, we propose SEP-YOLO, a novel framework that integrates a dual-domain collaborative mechanism for transparent object instance segmentation. Our method incorporates a Frequency Domain Detail Enhancement Module, which separates and enhances weak high-frequency boundary components via learnable complex weights. We further design a multi-scale spatial refinement stream, which consists of a Content-Aware Alignment Neck and a Multi-scale Gated Refinement Block, to ensure precise feature alignment and boundary localization in deep semantic features. We also provide high-quality instance-level annotations for the Trans10K dataset, filling the critical data gap in transparent object instance segmentation. Extensive experiments on the Trans10K and GVD datasets show that SEP-YOLO achieves state-of-the-art (SOTA) performance.

Index Terms—Transparent object, Instance segmentation, Frequency Domain, YOLO, Trans10K

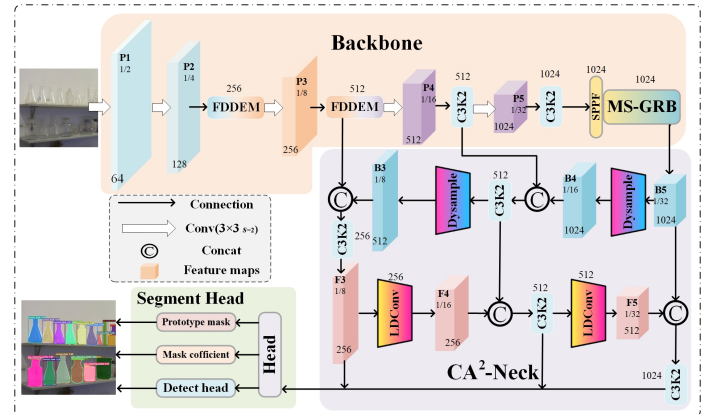
I. INTRODUCTION

Transparent objects, such as architectural glass windows, laboratory glassware, and drinking glasses, are ubiquitous in daily life. Accurate detection and segmentation of these objects are critical for diverse applications, such as robotic manipulation, autonomous driving, and industrial defect inspection [1]. While significant progress has been made in semantic segmentation of transparent objects [2]–[4], including Transformer-based Trans4Trans [5] and boundary-enhanced EBLNet [6], these methods inherently cannot distinguish between different instances of the same category [7], thus limiting their applicability in robotic grasping and industrial sorting [8]. In contrast, instance segmentation addresses this limitation by locating transparent object regions and delineating precise boundaries for each distinct instance [9].

Although numerous instance segmentation methods have been proposed [10]–[13], few are designed specifically for transparent objects. Transparent objects exhibit unique physical properties, including high light transmittance and low reflectivity. As a result, their appearance is strongly dependent on the background, with no distinctive texture or color features. Furthermore, complex light refraction results in severely

blurred boundaries that merge with the background [14]–[16], and these challenges lead to significant performance degradation in conventional instance segmentation models, which rely on strong appearance cues and clear boundaries.

Recently, Cherian et al. [17] proposed TrInSeg, a method that achieves data-efficient transparent instance segmentation under a few-shot setting using TransMixup data augmentation and template consistency filtering, and shows improved performance in robotic bin-picking tasks. However, this method relies on the assumption that transparent objects are rigid and regularly shaped, which considerably limits its generalization capability to non-rigid or irregular transparent objects.



- We provide high-quality instance-level annotations for the Trans10K dataset [18], filling the instance segmentation data gap for daily scenes. Our method achieves SOTA performance on both Trans10K and GVD while maintaining real-time inference speed, demonstrating strong potential for industrial applications.

II. PROPOSED METHOD

A. Frequency Domain Detail Enhancement Module

The inherent physical properties of transparent objects result in severely blurred boundaries, which manifest as high-frequency components with extremely low signal-to-noise ratio. These fragile details are easily diluted during convolution and pooling, leading to irreversible boundary information loss. To address this, we propose the Frequency Domain Detail Enhancement Module (FDDEM), which enhances frequency components corresponding to transparent object boundaries through learnable frequency domain complex weights. The refined components are then reintegrated into the spatial domain, providing clearer and more discriminative feature representations. FDDEM employs a dual-branch structure. The spatial context branch extracts and preserves multi-scale contextual information through convolutional layers, while the frequency detail branch first maps input features into the frequency domain using Fast Fourier Transform (FFT) [19]. The transformation is formulated as:

$$\mathcal{F}(\mathbf{X})(u, v) = \sum_{x=0}^{H-1} \sum_{y=0}^{W-1} \mathbf{X}(x, y) \cdot e^{-j2\pi\left(\frac{ux}{H} + \frac{vy}{W}\right)}, \quad (1)$$

where $\mathbf{X} \in \mathbb{R}^{H \times W \times C}$ denotes the input feature map, and $\mathcal{F}(\mathbf{X})$ represents its frequency domain representation.

We employ a multi-branch frequency enhancement strategy that adaptively modulates frequency domain features through learnable complex weight matrices. Unlike conventional high-pass filters with fixed frequency responses, our approach enables the network to autonomously discover optimal enhancement patterns tailored to the specific characteristics of transparent object boundaries. Each branch utilizes distinct complex weight matrices to adjust spectral components via element-wise multiplication, as illustrated in Fig. 2(a). The frequency enhancement process for each branch is defined as:

$$\mathcal{F}_{\text{enhanced}}^i = \mathcal{F}(\mathbf{X}) \odot \mathbf{W}^i, \quad (2)$$

where $\mathbf{W}^i \in \mathbb{C}^{C \times H \times W}$ are learnable complex weight matrices, and \odot denotes the Hadamard product. The real components of \mathbf{W}^i control amplitude modulation, while the imaginary components adjust phase relationships, providing comprehensive control over frequency domain characteristics.

These adaptively enhanced frequency components are transformed back to the spatial domain via Inverse Fast Fourier Transform (IFFT). The enhanced features from all branches are concatenated and compressed via a 1×1 convolution. A dual-attention mechanism then generates a frequency-guided attention map, which adaptively weights and enhances the

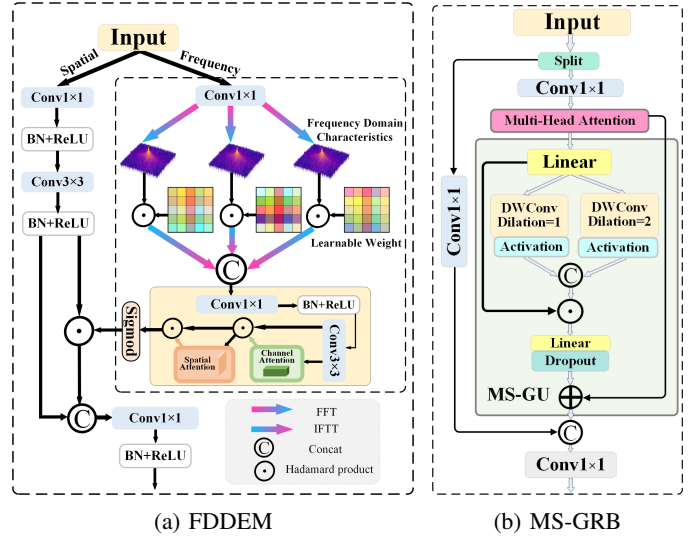


Fig. 2: Architecture of the proposed modules: (a) FDDEM; (b) MS-GRB

spatial features. The frequency-enhanced features are then integrated with the spatial branch. This integration operation connects the boundary-refined information from the frequency domain with the contextual representations from the spatial domain, forming a unified feature representation that combines enhanced boundary details with rich spatial context.

B. Multi-Scale Gated Refinement Block

While our FDDEM module enhances high-frequency boundaries in the frequency domain, features become diluted through spatial downsampling and aggregation, leading to a loss of boundary details and inaccurate localization in semantic features. To address this, we propose the Multi-scale Gated Refinement Module (MS-GRB) as shown in Fig. 2(b).

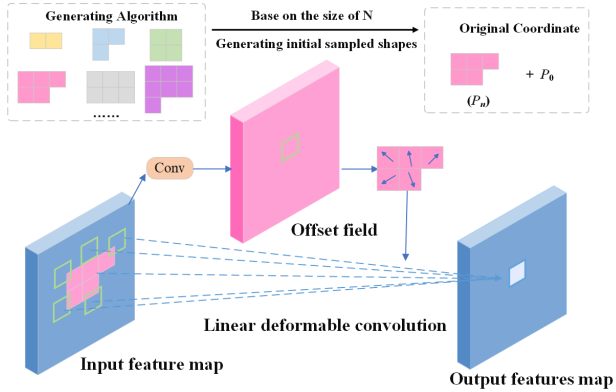
The core component is the Multi-scale Gating Unit (MS-GU), essentially a multi-scale variant of the Convolutional Gated Linear Unit (CGLU) [20]. It employs MSDWConv to aggregate multi-scale depthwise convolutions for efficient context extraction, while ensuring computational efficiency. As a multi-scale CGLU, it enhances the non-linear representation capability of spatially extracted features and optimizes cross-scale feature refinement; the gating mechanism [21] further performs adaptive channel-wise weighting and noise suppression on these refined features. The complete MS-GRB operation integrates MS-GU with residual learning:

$$\mathbf{Y} = \mathbf{X} + \text{Conv}_{1 \times 1}^{\text{shrink}}(\mathcal{D}_{\text{MS}}(\sigma_{\text{act}}(\mathbf{X}_k)) \odot \sigma_{\text{gate}}(\mathbf{V}_k)), \quad (3)$$

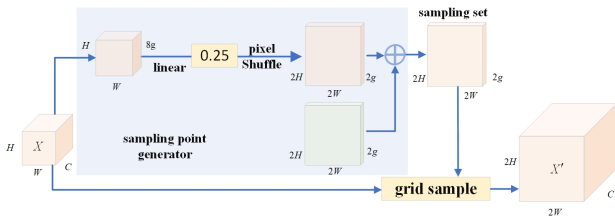
where \mathbf{X}_k and \mathbf{V}_k are feature branches from channel splitting, $\mathcal{D}_{\text{MS}}(\cdot)$ is MSDWConv, and $\sigma_{\text{act}}(\cdot)/\sigma_{\text{gate}}(\cdot)$ are activation and gating functions. This deep gated refinement enables MS-GRB to achieve precise localization and enhancement of faint boundary information at the deepest semantic level, significantly improving segmentation accuracy and generalization in complex backgrounds.

C. Content-Aware Alignment Neck

Due to the optical properties of transparent objects, boundaries appear blurred and spatial positions become unstable. In feature pyramid structures, both downsampling and upsampling operations face limitations: downsampling truncates feature information and reduces spatial details, while upsampling averages pixel values, diluting high-frequency boundary information and causing spatial misalignment. To address these challenges, we propose the Content-Aware Alignment Neck (CA²-Neck) with dual-path enhancements.



(a) Illustration of sampling position generation process in LDConv with $N=5$



(b) DySample with static scope factor

Fig. 3: (a) LDConv; (b) DySample

In the downsampling path, we employ the Linear Deformable Convolution (LDConv) to replace standard strided convolutions. As shown in Fig. 3(a), LDConv generates convolutional kernels with arbitrary numbers of parameters and arbitrary sampling shapes through a novel coordinate generation algorithm. This enables linear rather than quadratic parameter growth while maintaining representation capacity. The LDConv operation adapts to varying targets through learnable offsets that dynamically adjust sampling positions:

$$\mathbf{Y}_{\text{LDConv}} = \sum_{n=1}^N w_n \cdot x(\mathbf{P}_0 + \mathbf{P}_n + \Delta\mathbf{P}_n), \quad (4)$$

where N is the number of convolutional parameters, \mathbf{P}_n are the initial sampling coordinates generated by the algorithm, and $\Delta\mathbf{P}_n$ are the learned offsets. This formulation enables LDConv to capture extensive global context while preserving spatial details during downsampling, with parameter count growing linearly with kernel size rather than quadratically as in standard and deformable convolutions.

In the upsampling path, we adopt DySample [22], an innovative dynamic upsampler that reformulates the upsampling process from the perspective of point sampling as shown in Fig. 3(b). The core operation can be expressed as:

$$\mathbf{X}' = \text{grid_sample}(\mathbf{X}, \mathbf{G} + \lambda \cdot \text{linear}(\mathbf{X})), \quad (5)$$

where \mathbf{G} is the original sampling grid and $\lambda = 0.25$ is the static scope factor. This design employs bilinear initialization to ensure uniform distribution of initial sampling positions, while the scope factor constrains the offset range to prevent overlap between adjacent sampling points, effectively avoiding boundary artifacts and spatial misalignment. This mechanism enables DySample to adaptively adjust sampling positions based on feature content, generating semantically responsive sampling points in texture-rich edge regions to better preserve detailed information.

The dual-path enhancement collectively maintains boundary details and ensures accurate multi-scale feature alignment throughout the pyramid structure, particularly beneficial for transparent objects with blurred boundaries and unstable spatial positions.

III. EXPERIMENTS

A. Datasets

We evaluate SEP-YOLO on two representative transparent object datasets: GVD [23] and Trans10k [18]. The GVD dataset comprises 2,416 laboratory scenes, covering 14 classes of transparent chemical instruments. Since existing instance segmentation datasets lack coverage of common transparent household items, we utilized the Trans10K semantic segmentation dataset, adding instance-level annotations to adapt it for the instance segmentation task. This adapted dataset includes 9,491 images, encompassing two transparent object categories: glass surfaces and glassware. These two datasets collectively cover most scenarios encountered in daily life and professional laboratories. Comparison of SEP-YOLO with state-of-the-art detection methods demonstrates that SEP-YOLO achieves superior performance in transparent object segmentation.

B. Evaluation Metrics and Implementation Details

Evaluation metrics include Precision, Recall, and mean Average Precision (mAP) for both bounding boxes (box) and segmentation masks (mask). SEP-YOLO was implemented using PyTorch 2.7.1, with an input image size of 640×640 and a batch size of 4, trained for 300 epochs. The Stochastic Gradient Descent (SGD) optimizer was used, with an initial learning rate of 0.0001, employing a cosine learning rate scheduler and a 3-epoch warmup phase. All experiments were conducted on a server equipped with a NVIDIA RTX 4090 GPU and an Intel(R) Core(TM) i9-14900KF CPU.

C. Comparison with State-of-the-Art Methods

We compared SEP-YOLO with eight state-of-the-art methods, including YOLO11, on two benchmark datasets. As summarized in Table I, SEP-YOLO achieved the best performance on Trans10K, exceeding the second-best approach by

TABLE I: Performance comparison of different methods on Trans10k and GVD datasets. The best, second best, and third best results are highlighted in red, blue, and green, respectively.

Method	Venue	Box mAP_{50}		Box mAP_{75}		Mask mAP_{50}		Mask mAP_{75}		Params (M)	FPS
		Trans10k	GVD	Trans10k	GVD	Trans10k	GVD	Trans10k	GVD		
Mask-RCNN [10]	ICCV 2017	0.773	0.797	0.691	0.704	0.771	0.791	0.687	0.679	44.5	27
Solov2 [24]	NeurIPS 2020	0.803	0.856	0.601	0.642	0.805	0.852	0.600	0.621	36.1	43
YOLOv10n [25]	NeurIPS 2024	0.794	0.812	0.689	0.725	0.798	0.804	0.691	0.701	2.64	87
YOLO11n	-	0.816	0.851	0.742	0.751	0.813	0.849	0.729	0.742	2.87	97
TrInSeg [17]	IROS 2024	0.810	0.851	0.739	0.753	0.805	0.847	0.737	0.739	55.6	21
Hyper-YOLO-N [26]	TPAMI 2024	0.801	0.819	0.731	0.740	0.799	0.809	0.720	0.732	3.8	78
Mamba-YOLO-T [27]	AAAI 2025	0.791	0.854	0.727	0.760	0.787	0.850	0.719	0.733	6.3	69
YOLOv12n [28]	arxiv 2025	0.810	0.847	0.741	0.755	0.807	0.801	0.711	0.741	2.85	94
Ours		0.852	0.882	0.774	0.796	0.851	0.872	0.754	0.769	2.98	88

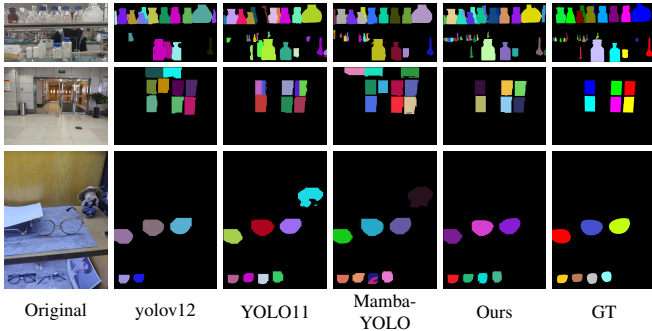


Fig. 4: Visual comparison of instance segmentation results on the GVD (first row) and Trans10K (second and third rows) datasets, respectively.

3.6% in Box mAP_{50} , 3.2% in Box mAP_{75} , 3.8% in Mask mAP_{50} , and 2.5% in Mask mAP_{75} . Consistent improvements were also observed on the GVD dataset across all metrics. These results confirm the effectiveness of SEP-YOLO in accurately identifying object boundaries and producing high-quality segmentation masks. In terms of efficiency, while YOLO11 remains the fastest and most compact, SEP-YOLO attains notably higher accuracy with only 0.23M additional parameters, thus maintaining a favorable balance between performance and complexity.

These results collectively demonstrate that SEP-YOLO effectively addresses the challenges of boundary blur and low contrast in transparent object segmentation, outperforming existing methods in both accuracy and generalization. The visual comparisons in Fig. 4 further highlight its ability to produce sharper boundaries and more complete masks, especially for transparent objects with complex background interactions.

D. Ablation Studies and Analysis

Ablation studies on Trans10K and GVD datasets validate each component of SEP-YOLO. As shown in Table II, the baseline achieved 0.816 Box mAP_{50} and 0.813 Mask mAP_{50} on Trans10K. Adding FDDEM alone improved Box mAP_{50} to 0.836 and Mask mAP_{50} to 0.833, demonstrating the significance of frequency domain enhancement for transparent object boundaries. Further incorporating MS-GRB or CA²-

TABLE II: Ablation study of SEP-YOLO components on the Trans10K dataset.

Method	Box		Mask	
	mAP_{50}	mAP_{75}	mAP_{50}	mAP_{75}
Baseline(YOLO11)	0.816	0.742	0.813	0.729
+ FDDEM	0.836	0.755	0.833	0.741
+ FDDEM + MS-GRB	0.845	0.759	0.841	0.749
+ FDDEM + CA ² -Neck	0.844	0.761	0.840	0.748
SEP-YOLO (ours)	0.852	0.774	0.851	0.754

TABLE III: Ablation study of SEP-YOLO components on the GVD dataset.

Method	Box		Mask	
	mAP_{50}	mAP_{75}	mAP_{50}	mAP_{75}
Baseline(YOLO11)	0.851	0.761	0.849	0.742
+ FDDEM	0.864	0.773	0.861	0.769
+ FDDEM + MS-GRB	0.870	0.784	0.863	0.758
+ FDDEM + CA ² -Neck	0.865	0.776	0.860	0.755
SEP-YOLO (ours)	0.882	0.796	0.872	0.769

Neck provided additional gains, with the full SEP-YOLO achieving the best performance of 0.852 Box mAP_{50} and 0.851 Mask mAP_{50} . Similar trends were observed on GVD (Table III). These results confirm the complementary role of each module in addressing the unique challenges of transparent object instance segmentation.

IV. CONCLUSION

In this paper, we propose SEP-YOLO to address low contrast and boundary blurring in transparent object instance segmentation under complex scenes. Comprehensive experiments on the challenging Trans10K and GVD datasets show that SEP-YOLO significantly outperforms existing SOTA methods in segmentation accuracy, while retaining a lightweight architecture and real-time inference speed. Furthermore, we contributed high-quality instance-level annotations for the Trans10K dataset, filling a critical data gap. The robust performance and high efficiency of SEP-YOLO thus demonstrate its significant potential for industrial and robotic applications.

REFERENCES

- [1] J. Jiang, G. Cao, J. Deng, T.-T. Do, and S. Luo, "Robotic perception of transparent objects: A review," *IEEE Transactions on Artificial Intelligence*, vol. 5, no. 6, pp. 2547–2567, 2024.
- [2] T. Sun, G. Zhang, W. Yang, J.-H. Xue, and G. Wang, "Trosd: A new rgb-d dataset for transparent and reflective object segmentation in practice," *IEEE Transactions on Circuits and Systems for Video Technology*, vol. 33, no. 10, pp. 5721–5733, 2023.
- [3] X. Yan, M. Sun, Y. Han, and Z. Wang, "Camouflaged object segmentation based on matching–recognition–refinement network," *IEEE Transactions on Neural Networks and Learning Systems*, vol. 35, no. 11, pp. 15993–16007, 2023.
- [4] S. Bharati, M. O. Ahmad, and M. N. S. Swamy, "Dual task learning: A semi-supervised approach to medical image joint segmentation and registration," in *2025 IEEE International Symposium on Circuits and Systems (ISCAS)*, pp. 1–5, 2025.
- [5] J. Zhang, K. Yang, A. Constantinescu, K. Peng, K. Müller, and R. Stiefelhagen, "Trans4trans: Efficient transformer for transparent object segmentation to help visually impaired people navigate in the real world," in *Proceedings of the IEEE/CVF International Conference on Computer Vision*, pp. 1760–1770, 2021.
- [6] H. He, X. Li, G. Cheng, J. Shi, Y. Tong, G. Meng, V. Prinet, and L. Weng, "Enhanced boundary learning for glass-like object segmentation," in *Proceedings of the IEEE/CVF International Conference on Computer Vision*, pp. 15859–15868, 2021.
- [7] J. Ruiz-Santaquiteria, G. Bueno, O. Deniz, N. Vallez, and G. Cristobal, "Semantic versus instance segmentation in microscopic algae detection," *Engineering Applications of Artificial Intelligence*, vol. 87, p. 103271, 2020.
- [8] M. Gualtieri and R. Platt, "Robotic pick-and-place with uncertain object instance segmentation and shape completion," *IEEE robotics and automation letters*, vol. 6, no. 2, pp. 1753–1760, 2021.
- [9] Y. Yan, Y. Hang, T. Hu, H. Yu, and F. Lai, "Visual slam in long-range autonomous parking application based on instance-aware semantic segmentation via multi-task network cascades and metric learning scheme," *SAE International Journal of Advances and Current Practices in Mobility*, vol. 3, no. 2021-01-0077, pp. 1357–1368, 2021.
- [10] K. He, G. Gkioxari, P. Dollár, and R. Girshick, "Mask r-cnn," in *Proceedings of the IEEE International Conference on Computer Vision*, pp. 2961–2969, 2017.
- [11] J. Zeng, H. Ouyang, M. Liu, L. Leng, and X. Fu, "Multi-scale yolact for instance segmentation," *Journal of King Saud University-Computer and Information Sciences*, vol. 34, no. 10, pp. 9419–9427, 2022.
- [12] C. Wei, H. Li, L. Chen, H. Zhou, O. Taukebayev, W. Wu, A. Temirbayev, L. Han, L. Ran, H. Yin, P. Wang, J. Liu, X. Zhang, and Y. Zhang, "River ice fine-grained segmentation: A gf-2 satellite image dataset and deep learning benchmark," *IEEE Transactions on Geoscience and Remote Sensing*, vol. 63, pp. 1–15, 2025.
- [13] J. Lee, W. Haixin, and Z. Jinjia, "Efficient cell segmentation and classification by leveraging an auto prompt generator and a new fine-tuning strategy," in *2025 IEEE International Symposium on Circuits and Systems (ISCAS)*, pp. 1–5, 2025.
- [14] D.-P. Fan, G.-P. Ji, M.-M. Cheng, and L. Shao, "Concealed object detection," *IEEE Transactions on Pattern Analysis and Machine Intelligence*, vol. 44, no. 10, pp. 6024–6042, 2022.
- [15] D.-H. Zhai, S. Yu, W. Wang, Y. Guan, and Y. Xia, "Tcrnet: Transparent object depth completion with cascade refinements," *IEEE Transactions on Automation Science and Engineering*, vol. 22, pp. 1893–1912, 2025.
- [16] D. Huo, J. Wang, Y. Qian, and Y.-H. Yang, "Glass segmentation with rgb-thermal image pairs," *IEEE Transactions on Image Processing*, vol. 32, pp. 1911–1926, 2023.
- [17] A. Cherian, S. Jain, and T. K. Marks, "Few-shot transparent instance segmentation for bin picking," in *2024 IEEE/RSJ International Conference on Intelligent Robots and Systems (IROS)*, pp. 5009–5016, IEEE, 2024.
- [18] E. Xie, W. Wang, W. Wang, M. Ding, C. Shen, and P. Luo, "Segmenting transparent objects in the wild," *CoRR*, vol. abs/2003.13948, 2020.
- [19] S. A. Magid, Y. Zhang, D. Wei, W.-D. Jang, Z. Lin, Y. Fu, and H. Pfister, "Dynamic high-pass filtering and multi-spectral attention for image super-resolution," in *Proceedings of the IEEE/CVF International Conference on Computer Vision*, pp. 4288–4297, 2021.
- [20] Z. Wang, "Glu attention improve transformer," *arXiv preprint arXiv:2507.00022*, 2025.
- [21] D. Shi, "Transnext: Robust foveal visual perception for vision transformers," in *Proceedings of the IEEE/CVF conference on computer vision and pattern recognition*, pp. 17773–17783, 2024.
- [22] W. Liu, H. Lu, H. Fu, and Z. Cao, "Learning to upsample by learning to sample," in *Proceedings of the IEEE/CVF International Conference on Computer Vision*, pp. 6027–6037, 2023.
- [23] J. Ge, X. Yang, M. Zhu, J. RAN, C. Zhai, and H. Zhang, "Instance segmentation of chemical transparent glassware in complex scene using aspp-solov2," *Journal of Chemical Engineering of Chinese Universities*, vol. 37, no. 6, pp. 962–970, 2023.
- [24] X. Wang, R. Zhang, T. Kong, L. Li, and C. Shen, "Solov2: Dynamic and fast instance segmentation," *Advances in Neural information processing systems*, vol. 33, pp. 17721–17732, 2020.
- [25] A. Wang, H. Chen, L. Liu, K. Chen, Z. Lin, J. Han, and G. Ding, "Yolov10: Real-time end-to-end object detection," in *Advances in Neural Information Processing Systems* (A. Globerson, L. Mackey, D. Belgrave, A. Fan, U. Paquet, J. Tomczak, and C. Zhang, eds.), vol. 37, pp. 107984–108011, Curran Associates, Inc., 2024.
- [26] Y. Feng, J. Huang, S. Du, S. Ying, J.-H. Yong, Y. Li, G. Ding, R. Ji, and Y. Gao, "Hyper-yolo: When visual object detection meets hypergraph computation," *IEEE Transactions on Pattern Analysis and Machine Intelligence*, 2024.
- [27] Z. Wang, C. Li, H. Xu, X. Zhu, and H. Li, "Mamba yolo: A simple baseline for object detection with state space model," in *Proceedings of the AAAI Conference on Artificial Intelligence*, vol. 39, pp. 8205–8213, 2025.
- [28] Y. Tian, Q. Ye, and D. Doermann, "Yolov12: Attention-centric real-time object detectors," *arXiv preprint arXiv:2502.12524*, 2025.